Supplementary Information

1. Derivation of I_{pd} equations

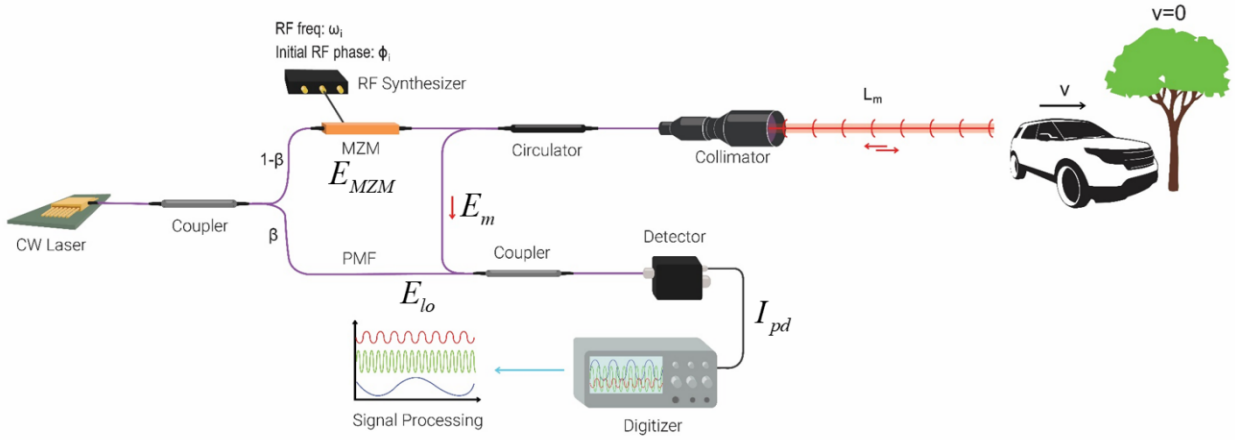

Fig.S1 | The schematic of PB-MTCW lidar system indicating the electric fields.

The electric fields of the local oscillator (E_{lo}) and the echo signal (E_m) are indicated on the PB-MTCW schematic in **Fig.S**1, as well as the transmission electric field after modulator (E_{MZM}) and the resultant photocurrent I_{pd}. The output of the CW laser is formulated as $E_{laser} = A_0 \exp(j\omega_0 t + j\phi_0)$, where $A_0 = \sqrt{P_{out}}$ is the amplitude, ω_0 is the angular frequency and ϕ_0 is the initial phase of the electric field generated by the source laser. The laser is then split into two by a coupler with a β/(1-β) power splitting ratio. The unmodulated local oscillator is formulated as in Eq.(S.1) by also considering fiber attenuation (α_f) and laser phase noise ($\phi_n(t-\tau_{lo})$), where τ_{lo} is the propagation time in the local oscillator branch.

$$E_{lo} = A_0 \alpha_f \sqrt{\beta} \exp(j\omega_0 t + j\phi_0 + j\phi_n(t-\tau_{lo})) \tag{S.1}$$

For simplicity, the phase induced to the optical carrier due to fiber path lengths is neglected. The light in the upper branch is modulated via a Mach-Zehnder electro-optic modulator (MZM). N number of phase-locked RF tones that have A_i^{RF} amplitude, ω_i angular frequency, and ϕ_i^{RF} initial phases generate the E-field as $E_{RF} = \sum_{i=1}^{N} A_i^{RF} \cos\left(\omega_i t + \phi_i^{RF}\right)$ that is further fed to the MZM for

modulation. Assuming a balanced MZM under push-pull configuration, the field transfer function can be formalized as $\cos\left(\frac{0.5\pi V_{in}}{V_\pi}\right)$ and at quadrature bias we have $V_{in}=\frac{V_\pi}{2}+E_{RF}$. As a result, we obtain $\cos\left(\frac{\pi}{4}+\frac{\pi}{2V_\pi}E_{RF}\right)=\frac{1}{\sqrt{2}}\left[\cos\left(\frac{\pi}{2V_\pi}E_{RF}\right)-\sin\left(\frac{\pi}{2V_\pi}E_{RF}\right)\right]$. The modulation depth of the MZM can be represented as $m=\frac{\pi A_i^{RF}}{V_\pi}$. Now, assuming a linear modulation with relatively low modulation depth to achieve the E-field after MZM by using $E_{MZM}=\frac{E_{laser}}{\sqrt{2}}-\frac{E_{laser}}{\sqrt{2}}\frac{\pi}{V_\pi}E_{RF}$ that is shown in Eq.(S.2).

$$E_{MZM}=\frac{A_0}{\sqrt{2}}\alpha_f\sqrt{1-\beta}\exp(j\omega_0 t+j\phi_0)-\frac{mA_0}{4\sqrt{2}}\alpha_f\sqrt{1-\beta}\sum_{i=1}^{N}\left(\begin{array}{l}\exp\left[j(\omega_0+\omega_i)t+j(\phi_0+\phi_i^{RF})\right]\\+\exp\left[j(\omega_0-\omega_i)t+j(\phi_0-\phi_i^{RF})\right]\end{array}\right) \quad \text{(S.2)}$$

After the formation of the sidebands, one can include the fiber path length traveled by the light to the total propagation distance, L_m, i.e. $L_m=L_{free}+n_{PMF}L_{fiber}$, where L_{free} is the light propagation in free space, n_{PMF} is the refractive index of the polarization-maintaining fiber, and L_{fiber} is the total fiber path length after MZM. Each modulation tone will accumulate a phase based on the L_m and speed of light, c, as $\phi_i^{range}=\frac{2L_m}{c}\omega_i$. The E-field of the echo signal is represented in Eq.(S.3) after defining the linear attenuation coefficient (α_m) related to the potential scattering, collection, and/or back coupling losses.

$$\begin{aligned}E_m=&\frac{A_0}{2\sqrt{2}}\alpha_m\alpha_f\sqrt{1-\beta}\exp\left[j\omega_0 t+j\phi_0+j\omega_0\frac{2L_m}{c}+j\phi_n(t-\tau)\right]\\&-\frac{mA_0}{4\sqrt{2}}\alpha_m\alpha_f\sqrt{1-\beta}\sum_{i=1}^{N}\left(\begin{array}{l}\exp\left[j(\omega_0+\omega_i)t+j\phi_0+j\phi_i^{RF}+j(\omega_0+\omega_i)\frac{2L_m}{c}+j\phi_n(t-\tau)\right]\\+\exp\left[j(\omega_0-\omega_i)t+j\phi_0-j\phi_i^{RF}+j(\omega_0-\omega_i)\frac{2L_m}{c}-j\phi_n(t-\tau)\right]\end{array}\right)\end{aligned} \quad \text{(S.3)}$$

Here, $\tau = 2L_m / c$ is the time of propagation and $\phi_n(t-\tau)$ is the laser phase noise related with τ that is when the laser beam first left the MZM. Since the defined phase noise term is related to the carrier, the same noise term will be carried by every modulation frequency.

The E_m and E_{lo} are combined via a combiner and the photocurrent is achieved based on the square-law detector as $I_{pd} = R\left(E_m + E_{lo}\right)\cdot\left(E_m + E_{lo}\right)^*$. The final I_{pd} after the interference of the local oscillator with the echo signal from a stationary target is shown in Eq.(S.4), where the laser phase noise difference of E_m and E_{lo} is represented as $\Phi\left(t,\tau,\tau_{lo}\right) = \phi_n(t-\tau_{lo}) - \phi_n(t-\tau)$.

$$
\begin{aligned}
I_{pd} = {} & RA_0^2\alpha_f^2\beta + \frac{3RA_0^2\alpha_m^2\alpha_f^2\left(1-\beta\right)}{16} + \frac{RA_0^2\alpha_m\alpha_f^2\sqrt{\beta}\sqrt{1-\beta}}{\sqrt{2}}\cos\left(\omega_0\frac{2L_m}{c} + \Phi\left(t,\tau,\tau_{lo}\right)\right) \\
& - \frac{RmA_0^2\alpha_m\alpha_f^2\sqrt{\beta}\sqrt{1-\beta}}{2\sqrt{2}}\left[\begin{array}{l}\displaystyle\sum_{i=1}^{N}\cos\left(\omega_i t + \left(\omega_0+\omega_i\right)\frac{2L_m}{c} + \phi_i^{RF} + \Phi\left(t,\tau,\tau_{lo}\right)\right) \\ \displaystyle+\sum_{i=1}^{N}\cos\left(\omega_i t - \left(\omega_0-\omega_i\right)\frac{2L_m}{c} - \phi_i^{RF} - \Phi\left(t,\tau,\tau_{lo}\right)\right)\end{array}\right] \\
& + \frac{RmA_0^2\alpha_m^2\alpha_f^2\left(1-\beta\right)}{8}\left[\sum_{i=1}^{N}\cos\left(\omega_i t + \omega_i\frac{2L_m}{c} + \phi_i^{RF}\right) + \sum_{i=1}^{N}\cos\left(\omega_i t + \omega_i\frac{2L_m}{c} - \phi_i^{RF}\right)\right] \\
& + \frac{Rm^2A_0^2\alpha_m^2\alpha_f^2\left(1-\beta\right)}{8}\sum_{i=1}^{N}\cos\left(2\omega_i t + \omega_i\frac{4L_m}{c}\right)
\end{aligned}
\tag{S.4}
$$

In the case of a dynamic target, the backscattered light will realize a Doppler frequency shift of ω_d. The Doppler shift is related to the target speed as $\omega_d = (2v/c)\omega_0$, where v is the target velocity in the direction of laser propagation. Similarly, each modulation frequency realizes a Doppler shift ω_d^i, as well. The returned signal E-field after collection is shown in Eq.(S.5).

$$E_m = \frac{A_0}{2\sqrt{2}}\alpha_m\alpha_f\sqrt{1-\beta}\exp(j(\omega_0+\omega_d)t + j\omega_0\frac{L_m}{c} + j(\omega_0+\omega_d)\frac{L_m}{c} + j\phi_0 + j\phi_n(t-\tau))$$
$$-\frac{mA_0}{4\sqrt{2}}\alpha_m\alpha_f\sqrt{1-\beta}\sum_{i=1}^{N}\left(\begin{array}{l}\exp\left[\begin{array}{l} j(\omega_0+\omega_i+\omega_d+\omega_d^i)t + j(\omega_0+\omega_i)\frac{L_m}{c} \\ +j(\omega_0+\omega_i+\omega_d+\omega_d^i)\frac{L_m}{c} + j(\phi_0+\phi_i^{RF}) + j\phi_n(t-\tau)\end{array}\right] \\ +\exp\left[\begin{array}{l} j(\omega_0-\omega_i+\omega_d-\omega_d^i)t + j(\omega_0-\omega_i)\frac{L_m}{c} \\ +j(\omega_0-\omega_i+\omega_d-\omega_d^i)\frac{L_m}{c} + j(\phi_0-\phi_i^{RF}) + j\phi_n(t-\tau)\end{array}\right]\end{array}\right) \quad \text{(S.5)}$$

The forward propagating and backscattered light acquire different phases during their propagation due to change in the carrier and modulation frequencies. Since $\omega_0 >> \omega_i$, it is possible to assume $\omega_d + \omega_d^i \simeq \omega_d - \omega_d^i \simeq \omega_d$. Unless the target is moving at extreme velocities, this assumption is always true for most practical applications. Therefore, the resultant I_{pd} of a moving target is given in Eq.(S.6).

$$\begin{aligned} I_{pd} &= R\beta A_0^2\alpha_f^2 + \frac{R(1-\beta)A_0^2\alpha_m^2\alpha_f^2}{8} + \frac{Rm(1-\beta)A_0^2\alpha_m^2\alpha_f^2}{16} \\ &+ \frac{Rm\sqrt{\beta}\sqrt{(1-\beta)}A_0^2\alpha_m\alpha_f^2}{\sqrt{2}}\cos\left(\omega_d t + \frac{2L_m}{c}\omega_o + \frac{L_m}{c}\omega_d + \Phi(t,\tau,\tau_{lo})\right) \\ &- \frac{Rm(1-\beta)A_0^2\alpha_m^2\alpha_f^2}{8}\sum_{i=1}^{N}\cos\left(\omega_i t + \frac{2L_m}{c}\omega_i + \phi_i^{RF}\right) \\ &+ \frac{Rm(1-\beta)A_0^2\alpha_m^2\alpha_f^2}{16}\sum_{i=1}^{N}\cos\left(2\omega_i t + \frac{4L_m}{c}\omega_i\right) \\ &- \frac{Rm\sqrt{\beta}\sqrt{(1-\beta)}A_0^2\alpha_m\alpha_f^2}{2\sqrt{2}}\sum_{i=1}^{N}\cos\left((\omega_i+\omega_d)t + \frac{2L_m}{c}(\omega_o+\omega_i) + \frac{L_m}{c}\omega_d + \phi_i^{RF} + \Phi(t,\tau,\tau_{lo})\right) \\ &- \frac{Rm\sqrt{\beta}\sqrt{(1-\beta)}A_0^2\alpha_m\alpha_f^2}{2\sqrt{2}}\sum_{i=1}^{N}\cos\left((\omega_i-\omega_d)t - \frac{2L_m}{c}(\omega_o-\omega_i) - \frac{L_m}{c}\omega_d - \phi_i^{RF} - \Phi(t,\tau,\tau_{lo})\right) \end{aligned} \quad \text{(S.6)}$$

2. Triangulation Algorithm Details

The triangulation algorithm is used after calculating the $L_0^{i,j} = c\Delta\phi_{i,j}/\Delta\omega_{i,j}$ from the phase variation of the individual tones to determine the actual value of the target distance L_m. It is possible to generate a total of $\binom{N}{2}$ possible $L_0^{i,j}$ for a stationary target, whereas the targets in motion will

yield $\binom{2N}{2}$ degrees of freedom. The final estimated L_m values should converge to the same value for each integer n based on $L_m = L_0^{i,j} + nL^{i,j}$, where $L^{i,j} = 2\pi c / \Delta\omega_{i,j}$. Here, we set the maximum anticipated range of a target by selecting the maximum value of n. In practice, this range is determined by the optical system loss or the application. Then, the integer value of n is scanned from n = 1 to n_{max} and all the estimated L_m are concatenated in a data matrix $M_{k,l}$, where k is equal to n_{max} and l is the number of available $\Delta\omega_{i,j}$, also corresponding L_m for each $\Delta\omega_{i,j}$ are placed in an increasing fashion to each column. An example of the data matrix $M_{k,l}$ is given in Fig.S2 after acquiring data with a 3-tone PB-MTCW lidar. Finally, the standard deviation of each row is computed as $\sigma_k = \sqrt{\sum_{r=1}^{l}\left(M_{k,r} - \overline{M}_k\right)^2 / l}$, where $\overline{M}_k$ is the mean value of the k^{th} row.

		l		
		$\omega_3 - \omega_2$	$\omega_3 - \omega_1$	$\omega_2 - \omega_1$
	1	$k = 1$	$k = 1$	$k = 1$
	2	$k = 2$	repeat	repeat
	3	$k = 3$	repeat	repeat
	4	$k = 4$	repeat	repeat
	⋮	⋮	repeat	k = 2-10
	300	$k = 300$	$k = 2$	$k = 11$
k	**301**	$k = 301$	repeat	repeat
	302	$k = 302$	repeat	repeat
	⋮	⋮	$k = 3$	k = 12-17
	498	$k = 498$	repeat	$k = 18$
	499	$k = 499$	repeat	repeat
	500	$k = 500$	repeat	repeat

Fig.S2 | Illustration of data matrix $M_{k,l}$ for a 3-tone PB-MTCW lidar with ω_1, ω_2, and ω_3. The k values in the matrix represent the value of n in $L_m = L_0^{i,j} + \left(2\pi nc / \Delta\omega_{i,j}\right)$. The repetitive terms, where the k values are equal in the consecutive rows are indicated in the matrix as repeat.

3. Simulation Results

As discussed in the Results section, there are several local minima points along with the global minimum. We suggest increasing the number of phase-locked RF modulation frequencies. In particular, adding extra low-frequency tones will reduce error, and adding extra high frequencies will improve the resolution. We performed a numerical simulation to show the impact of the number of modulation tones and the results are presented in Fig.S3. Here, we used three modulation tones at 500, 700, and 950MHz in the first simulation. Then we increased the number of tones to 6 by introducing 20, 670, and 890MHz. As shown in Fig.S3.a, a limited number of tones yield local minima points together with the global minimum. However, increasing the number of tones and utilizing a low modulation tone such as 20MHz with larger $L^{i,j}$ will eliminate the potential local minima points due to increasing σ_k values, thus enhances the triangulation algorithm. It is important to note we assume that all frequency tones are harmonics of a 10MHz common source, and they are also all phase-locked to this source. Fig.S4 demonstrates the ranging of multiple target distances of L_m=1, 2, and 3m by using PB-MTCW lidar with 6 tones.

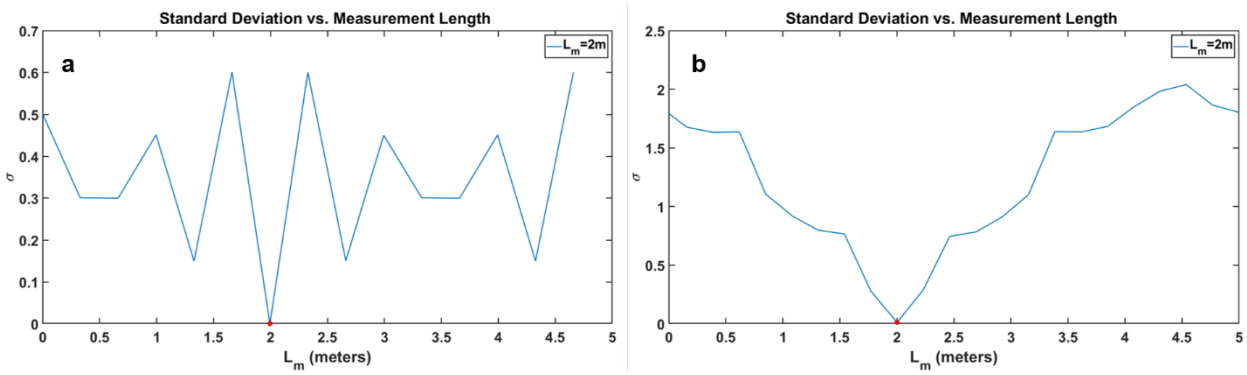

Fig.S3 | Simulation results of stationary target ranging at Lm = 2m. a. Simulation result of ranging after triangulation algorithm using 3 modulation tones at 500, 700, and 950MHz. **b.** Simulation result of ranging after triangulation algorithm using 6 modulation tones at 20, 500, 670, 700, 890, and 950MHz.

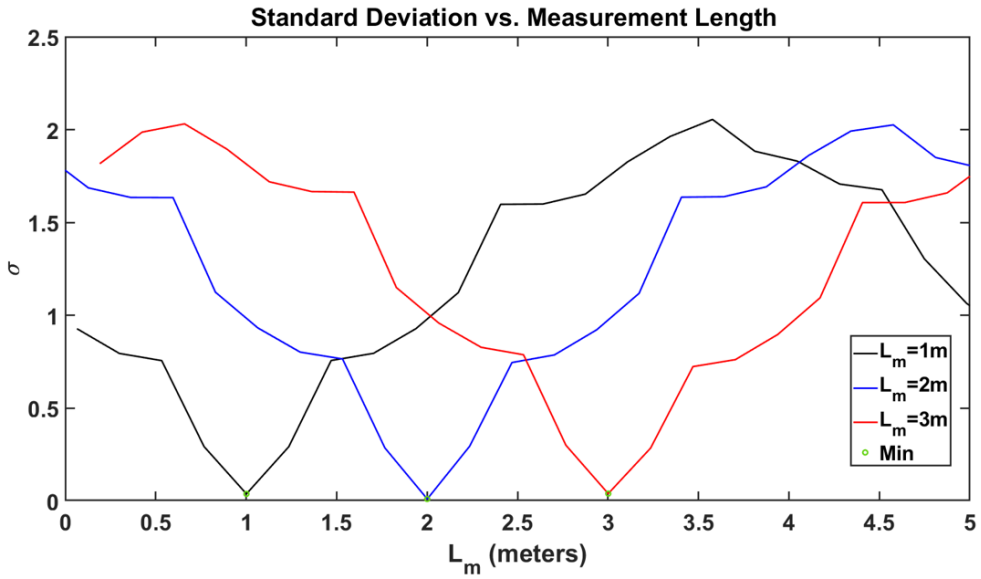

Fig.S4 | Simulation results demonstrating the L_m triangulation with acquired tone phases. Numerical simulation results demonstrating the capability of the triangulation algorithm with 6 modulation tones. Digital signal processing is performed to compute the resultant tone phases according to the signal processing flowchart. Triangulation results for three stationary target positions of L_m = 1, 2, and 3m are represented with different colors as black, blue, and red, respectively. The x-axis values of the minimum standard deviation (σ) points correspond to the distances of the target that are indicated with green circles.

4. Extended Experimental Results

The experimental results of the dynamic target ranging and velocimetry during the measured 10 trials are tabulated in Table S1.

Table S1 |

High Coherence Laser		Low Coherence Laser	
Range (cm)	**Velocity (cm/s)**	**Range (cm)**	**Velocity (cm/s)**
101.18	10.51	102.68	10.51
98.44	10.51	100.74	10.24
101.18	9.98	101.01	9.98
102.01	9.44	104.91	10.51
97.29	9.98	96.84	9.98
100.93	10.24	102.52	10.24
101.61	11.31	103.40	9.18
98.83	9.98	104.7	11.31
95.97	10.24	108.45	10.24
92.33	10.51	100.07	9.71

Simultaneous ranging and velocimetry results of a dynamic target with high and low coherence lasers.

Results of the triangulation algorithm during stationary target ranging while the target is at L_1, L_2, and L_3 with high coherence and low coherence laser is given in Fig. S5.

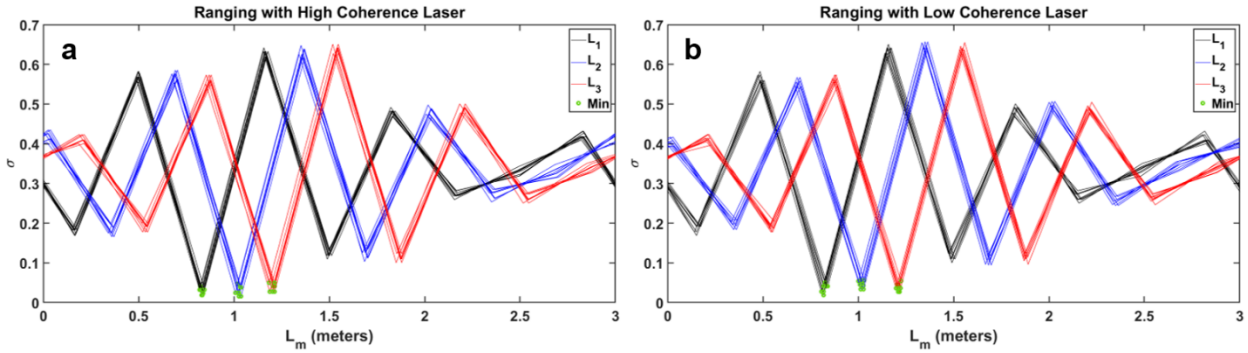

Fig. S5 | Complete stationary target ranging results with high and low coherence lasers via PB-MTCW technique. Three measurement distances are L_1~83cm, L_2~103cm, and L_3~121cm for stationary target ranging. **a.** Stationary target ranging results of 10 trials for three different positions using the narrow linewidth laser. **b.** Stationary target ranging results of 10 trials for three different positions using the temporally incoherent light source.

In addition, the results of stationary target ranging at three different locations are presented in Table S2 with the corresponding mean and standard deviation values.

Table S2 | Ranging results of a stationary target with high and low coherence lasers.

	High Coherence Laser			Low Coherence Laser		
	Range @ L_1 (cm)	**Range @ L_2 (cm)**	**Range @ L_3 (cm)**	**Range @ L_1 (cm)**	**Range @ L_2 (cm)**	**Range @ L_3 (cm)**
	82.70	102.59	121.29	83.23	100.85	120.35
	82.31	102.19	118.79	83.94	103.07	122.17
	83.38	101.83	120.62	80.69	102.71	120.62
	83.06	103.66	121.33	82.16	102.67	121.34
	81.99	103.66	120.97	83.23	100.10	120.94
	84.49	103.30	118.43	82.47	101.64	122.45
	83.02	102.19	120.22	81.80	101.29	121.66
	83.06	102.55	120.22	81.80	102.71	119.83
	83.42	103.66	121.29	81.76	100.85	120.90
	83.82	100.76	121.29	81.80	102.04	122.17
Average	83.13	102.64	120.44	82.29	101.79	121.24
Standard deviation	0.72	0.95	1.06	0.95	1.00	0.87